Research Square

Preprints are preliminary reports that have not undergone peer review.
They should not be considered conclusive, used to inform clinical practice,
or referenced by the media as validated information.

BMS constrained PSO optimized multistage fast charging of an electric vehicle battery in a PV grid hybrid DC charging station

Ankita Singh
Sharda University
Manisha Rajoriya
manisha.rajoriya@sharda.ac.in

Sharda University
Suman lata Dhar
Sharda University

Research Article

Keywords: Electric vehicle fast charging, Battery management system, Particle swarm optimization, Multistage constant current charging, PV grid hybrid charging station, Power quality

Posted Date: November 11th, 2026

DOI: https://doi.org/10.21203/rs.3.rs-11358259/v1

License: This work is licensed under a Creative Commons Attribution 4.0 International License.
Read Full License

Additional Declarations: No competing interests reported.

BMS constrained PSO optimized multistage fast charging of an electric vehicle battery in a PV grid hybrid DC charging station

Ankita Singh[1], Manisha Rajoriya[2*], Sumanlata Dhar[3]

[1 2 3*]Department of Electrical, Electronics and Communication Engineering, Sharda University, Greater Noida, Uttar Pradesh, India.

*Corresponding author(s). E-mail(s): manisha.rajoriya@sharda.ac.in;
Contributing authors: 2024105771.ankita@dr.sharda.ac.in;
suman.lata@sharda.ac.in;

Abstract

Fast charging of electric vehicles (EVs) is limited by the cell voltage and temperature limits enforced by the battery management system (BMS), while hybrid charging stations must also keep grid power quality within standards. This paper presents a BMS constrained multistage constant current (MSCC) charging algorithm optimized by particle swarm optimization (PSO) for a PV grid hybrid DC fast charging station. The station, modelled in MATLAB/Simulink, comprises a unity power factor front end converter, an isolated DC to DC charger, a 14.4 kWp photovoltaic array with perturb and observe maximum power point tracking (MPPT) on an 800 V DC link, and a 54 Ah pack of temperature dependent cells with cell to cell variation. The BMS combines four current stages, a 4.2 V constant voltage loop on the highest cell and thermal derating between 40 and 45 °C; PSO tunes the stage currents and state of charge breakpoints. The optimized profile charges the pack from 20 % to 80 % in 22.6 min, 38.1 % faster than 1C constant current constant voltage (CCCV) charging and 6.1 % faster than CCCV at equal peak current, with all cells below 4.201 V and 43.5 °C. At 45 °C ambient the reduction reaches 29.8 %. Rerating the front end converter lowers the grid current total demand distortion from 9.71 % to 2.66 % (2.91 % with PV), a power factor of 0.991. The MPPT extracts over 98.2 % of the available PV power, supplying up to 34.9 % of the station input without affecting the charging current.

Keywords: Electric vehicle fast charging, Battery management system, Particle swarm optimization, Multistage constant current charging, PV grid hybrid charging station, Power quality

1 Introduction

1.1 Background

The rapid growth of electric vehicles (EVs) has made the charging station a critical interface between the vehicle battery and the power grid. DC fast charging stations, typically rated from tens to hundreds of kilowatts, must charge the battery quickly while drawing a clean current from the grid [1]. Reviews of charging technology report that a practical fast charger should bring the battery to about 80 % state of charge (SOC) in roughly 30 minutes [2], and modular architectures have been proposed to scale such stations to ultra fast levels [3]. The energy management schemes used in charging stations [4], the bidirectional charger topologies needed for vehicle to grid operation [5] and the DC to DC converters that form the core of every DC charger [6, 7] have been surveyed recently, including in this journal.

Supplying charging stations from renewable sources reduces their grid demand and carbon footprint. Solar powered EV charging has been reviewed from the technical [8] and techno economic [9] points of view. A 4 kW solar power based hybrid charging station was designed and simulated in [10], which serves as the grid power quality, maximum power point tracking (MPPT) efficiency or charging time.

1.2 Literature review

PV and hybrid charging stations. The feasibility of grid connected solar wind stations was analysed in [11], where a renewable fraction of 0.87 was reported. Stations combining PV, battery storage and diesel generation [12], grid connected PV with battery energy storage [13], distributed energy resources with seamless grid connection [14] and hybrid converter topologies for PV grid EV integration [15] have been demonstrated. Transactive energy between PV farms and charging stations [16] and disturbance observer based sliding mode control of the DC voltage in solar stations [17] have also been proposed. At smaller power levels, an off grid PV station with an interleaved three port converter achieved 95.5 % efficiency [18], and an integrated Zeta Luo converter was used for solar EV charging [19]. Metaheuristic MPPT for grid tied stations [20], techno economic optimization of PV powered stations for Indian climates [21], solar wind DC microgrids for desert regions [22] and combined hydrogen and EV stations [23] extend this line of work.

Planning and scheduling. Another group of studies addresses where and when EVs are charged consensus based power sharing between the grid and stations [24], the location and sizing of solar assisted stations [25, 26], uncertainty in distribution systems with correlated EV demand and renewable generation [27], infrastructure planning around transit hubs [28] and deep learning prediction of charging demand with 97.1 % accuracy [29].

DC fast charging and converter control Battery enabled DC fast charging stations and their grid integration were studied in [30, 31]. A fast charging station on a DC microgrid using multistage constant current (MSCC) charging reached about 30 min charging times [32]. Grid forming inverters for charging stations [33], model predictive control of three level converters in bipolar DC microgrids [34], a PSO tuned

sliding mode controller for bidirectional DC to DC converters [35], an artificial neural network controlled converter with THD below 2 % and power factor above 0.98 [36] and a wireless charger with a multilevel power factor correction front end [37] show the variety of converter level solutions.

Power quality Large EV loads distort the grid current a review in [38] reports harmonic distortion rising from 3 % to 28 % over a charging cycle. A comparison of DC fast charger topologies found a grid current THD of 7.89 % for the full bridge charger [39], while a model predictive PV integrated charger reached 0.96 % THD and a charging current ripple below 2.5 % at 10 kW [40]. Adaptive filter control [41] and unified power quality conditioners [42] have been applied to renewable fed stations. Compliance is normally judged [43].

Battery, BMS and charging protocols. The behaviour of lithium-ion cells depends on chemistry, temperature and SOC, and accurate SOC estimation is central to battery management [44, 45]. The charging protocol itself determines how fast and how safely the battery is charged. A PSO optimized multi stepped CCCV controller reduced the charging time by 31.2 % compared with CCCV [46], and a genetic algorithm multistage strategy with temperature rise control reduced the charging time by 1.9 to 9.54 % at 10 to 40 °C [47]. PSO [48] is widely used for such problems because it needs only the value of the objective function.

Table 1 summarises the most closely related studies.

Table 1: Comparison of related studies with this work (✓ = addressed; – = not the focus of the study)

Ref.	System studied	PV–grid hybrid	Charging-profile optimization	Cell-level BMS limits	Grid power quality	Key reported result
[10]	4 kW solar hybrid EV station	✓	–	–	–	design and simulation; no THD, MPPT efficiency or charging time
[11]	Solar–wind grid-connected station	✓	–	–	–	renewable fraction 0.87
[18]	Off-grid PV three-port converter	PV only	–	–	–	95.5 % efficiency

Ref.	System studied	PV–grid hybrid	Charging-profile optimization	Cell-level BMS limits	Grid power quality	Key reported result
[32]	Fast-charging station on DC microgrid	DC micro-grid	MSCC	–	–	≈ 30 min fast charge
[35]	PSO-tuned SMC DC-DC converter	–	controller tuning	–	near-unity PF	CC→CV transition 0.37 s
[36]	ANN-controlled converter, 350 W	–	–	–	✓	THD < 2 %, PF > 0.98
[39]	DC fast-charger topologies, 80 kW	–	–	–	✓	full-bridge THD 7.89 %
[40]	MPC PV-integrated charger, 10 kW	✓	–	–	✓	THD 0.96 %, ripple < 2.5 %
[46]	PSO multi-stepped CC-CV	–	✓ (PSO)	heat	–	-31.2 % time vs CC-CV (to 100 %)
[47]	GA multistage charging	–	✓ (GA)	temperature rise	–	-1.9 to -9.54 % time vs CC-CV
This work	**60 kW DC fast charger + 14.4 kWp PV**	✓	**✓ (PSO, 7 variables)**	**✓ (4.2 V, 45 °C, per cell)**	**✓ (TDD 2.66 %)**	**22.6 min, -38.1 % vs 1C CC-CV**

1.3 Research gap

Table 1 shows that the literature treats the problem in separate parts. Charging protocol studies [46, 47] optimize the current profile of a single cell or battery but do not model the charger, the grid or a renewable source. Charger and power quality studies

[36, 39, 40] model the converter and its grid current but charge the battery with a fixed current. Hybrid station studies [10, 11, 18] focus on sizing, efficiency and energy sharing. None of the compared works optimizes the charging profile under cell level BMS limits inside a PV grid hybrid fast charger while also verifying grid code power quality. The base study [10] reports no power quality, MPPT or charging time results.

1.4 Contributions

The main contributions of this paper are

1. A switching level model of a PV grid hybrid DC fast charging station with a realistic 99s2p, 54 Ah pack of temperature dependent cells with cell to cell variation, built from validated MathWorks components [49–51] with a corrected pack scaling method and cell level BMS signals.
2. A redesign of the front end converter for the actual charging power, which reduces the grid current total demand distortion (TDD) from 9.71 % to 2.66 % and satisfies the limit [43], with and without PV.
3. A BMS constrained MSCC charging algorithm with a constant voltage loop on the highest cell and thermal derating, whose four stage currents and three SOC breakpoints are optimized by PSO; the resulting profile charges from 20 % to 80 % SOC in 22.6 min within the 4.2 V and 45 °C limits.
4. A combined evaluation of charging time, cell temperature and voltage, ageing stress, ambient temperature (25 to 45 °C), MPPT efficiency, renewable share and grid power quality, with a quantitative comparison against published work.

1.5 Organization of the paper

Section 2 describes the charging station. Section 3 presents the mathematical models, and Section 4 the proposed BMS charging algorithm and its PSO optimization. Section 5 gives the simulation set up and the performance indices. Section 6 presents and discusses the results and compares them with published work. Section 7 states the limitations and future scope, and Section 8 concludes the paper.

2 System description

2.1 Station architecture

Fig. 1 shows the studied station. A three-phase voltage source front end converter (FEC) rectifies the 415 V, 50 Hz grid through an L filter and regulates an 800 V DC link at unity displacement power factor. A 14.41 kWp PV array feeds the same DC link through a 10 kHz boost converter with perturb and observe (P&O) MPPT. An isolated DC-DC converter, consisting of a 10 kHz full bridge inverter, a high frequency transformer (ratio 1 : 0.5), a diode rectifier and a 5 mH output inductor, charges the battery pack. The BMS reads the voltage, temperature and SOC of every cell and sets the charging current reference the stage currents of the BMS are tuned offline by PSO. The FEC, the DC to DC converter and the battery module are based on the

MathWorks DC fast charger [49] and temperature dependent battery module [50], and the PV sub system on the MathWorks PV, MPPT boost [51].

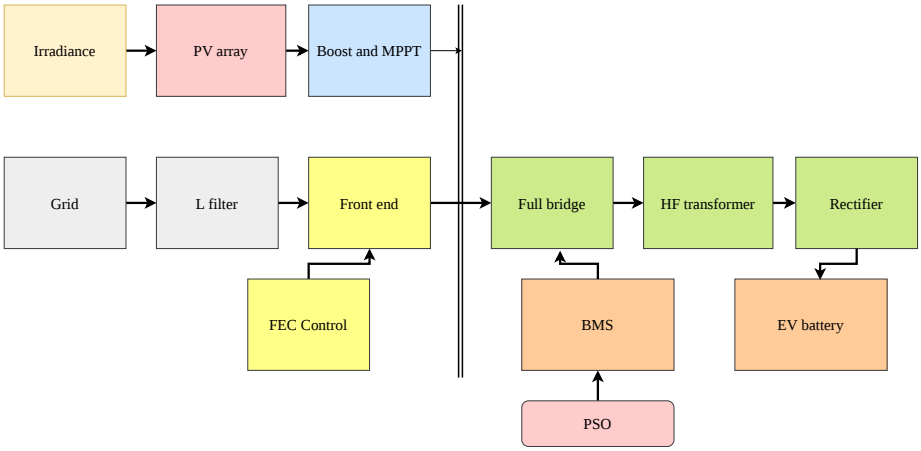


Fig. 1 Architecture of the PV grid hybrid DC fast charging station with BMS and offline PSO

2.2 Battery pack

The pack consists of 27 Ah pouch cells represented by an equivalent circuit model with SOC and temperature dependent open circuit voltage (OCV) and series resistance R_0 (7 SOC $\times$ 3 temperature look up tables; R_0 = 8.2–11.7 mΩ). Two cells form a parallel assembly, three assemblies form a 3s2p module, and 33 modules in series form a 99s2p, 54 Ah pack with an OCV range of about 346 to 415 V (Fig. 2). Capacity deviations of [5, -1, -3, -2, 4, 1] % and SOC or temperature-dependent R_0 deviations on cells 1 and 3 make the cells of a module unequal, as in a real pack. Each cell has a thermal mass of 900 J/K (0.8 kg $\times$ 1100 J kg^{-1} K^{-1}), a 0.5 K/W path to the module and a convective path (h = 100 W m^{-2} K^{-1}, A = 0.04 m^2) to the ambient.

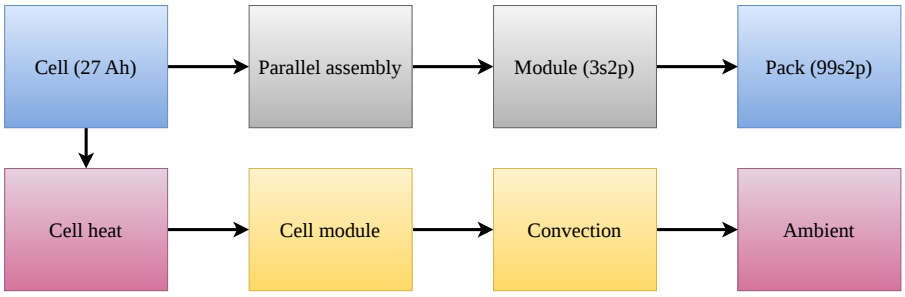


Fig. 2 Battery structure cell, parallel assembly, 3s2p module and 99s2p pack, with the thermal path from cell heat to ambient

3 Mathematical modelling

3.1 Grid and front end converter

With the phase-locked loop aligning the d-axis to the grid voltage ($v_q = 0$), the converter and filter are described in the synchronous frame by

$$L\frac{di_d}{dt} = v_d - R\,i_d + \omega L\,i_q - v_{cd}, \qquad L\frac{di_q}{dt} = v_q - R\,i_q - \omega L\,i_d - v_{cq} \tag{1}$$

$$P = \frac{3}{2}\left(v_d i_d + v_q i_q\right), \qquad Q = \frac{3}{2}\left(v_q i_d - v_d i_q\right) \tag{2}$$

$$C_{dc}\frac{dV_{dc}}{dt} = i_{dc,FEC} + i_{dc,PV} - i_{dc,DCDC} \tag{3}$$

where L and R are the filter inductance and resistance, v_{cd} and v_{cq} the converter voltages and $C_{dc} = 20$ mF the DC-link capacitance. An outer PI loop regulates V_{dc} and produces i_d^*; $i_q^* = 0$ gives unity displacement power factor. Each PI controller has the form $u = K_p\left(e + \frac{1}{T_i}\int e\,dt\right)$, with gains from the technical and symmetric optimum rules of [49]:

$$K_{p,i} = \frac{L}{2\,G\,K_s\,T_\varphi}, \quad T_{i,i} = \frac{L}{R}, \quad G = \frac{V_{dc}}{2}, \quad T_\varphi = \frac{1}{2f_{sw}} + T_s \tag{4}$$

$$K_{p,v} = \frac{C_{dc}\,K_s}{2\,K\,K_{s,v}\,T_{del}}, \quad T_{i,v} = 4T_{del}, \quad K = \frac{\widehat{V}_{ph}}{V_{dc}}, \quad T_{del} = 2T_\varphi + T_{s,v} \tag{5}$$

The admissible line inductance for a rated peak AC current $\widehat{I}_{ac}$ is

$$L_{\max} = 0.95\,\frac{V_{dc}/2 - V_{LL}\sqrt{2/3}}{\omega\,\widehat{I}_{ac}}, \qquad \widehat{I}_{ac} = \frac{\sqrt{2}\,I_{dc}\,V_{dc}}{\sqrt{3}\,V_{LL}} \tag{6}$$

The original rated for $I_{dc} = 700$ A (≈ 560 kW), which gives $L_{\max} = 0.17$ mH. For the actual charging power the FEC was re-rated to 75 A (60 kW), giving $L_{\max} = 1.57$ mH; the selected inductance is 0.3 mH (Section 6.2), with $K_{p,i} = 0.00625$ and $T_{i,i} = 15$ ms (original 0.00208 and 5 ms), $K_{p,v} = 181.6$ and $T_{i,v} = 0.52$ ms.

3.2 Isolated DC to DC converter

The full bridge applies a square wave voltage to the transformer of ratio $n = 0.5$. The average output voltage and the charging current are

$$V_o \approx 2\,n\,D\,V_{dc}, \quad 0 \le D \le 0.5, \qquad L_o\frac{di_{bat}}{dt} = V_o - v_{pack} \tag{7}$$

and the duty ratio is set by a PI current controller, $D = K_p e + K_i\int e\,dt$ with $e = I_{ref} - i_{bat}$, $K_p = 2$ and $K_i = 1$.

3.3 Battery cell, module and pack

For cell j (charging current positive),

$$\begin{aligned} v_{cell,j} &= OCV(SOC_j, T_j) + i_j R_{0,j}(SOC_j, T_j), \\ SOC_j(t) &= SOC_0 + \frac{1}{3600 Q_j} \int_0^t i_j \, dt. \end{aligned} \tag{8}$$

$$Q_j = Q\left(1 + \frac{\delta Q_j}{100}\right), \qquad R_{0,j} = R_0\left(1 + \frac{\delta R_j}{100}\right) \tag{9}$$

$$mc_p \frac{dT_j}{dt} = i_j^2 R_{0,j} - \frac{T_j - T_{node}}{R_c}, \qquad T_{node} - T_{amb} = Q_{node}\,\frac{1}{hA} \tag{10}$$

The two cells of a parallel assembly share the assembly current so that their terminal voltages are equal. The pack is formed from one simulated module by a voltage controlled voltage source and a current controlled current source

$$v_{pack} = v_{mod} - K_s v_{mod}, \quad K_s = -\left(N_s - 1\right) \;\Rightarrow\; v_{pack} = N_s\, v_{mod}, \quad N_s = 33 \tag{11}$$

The gain $K_s = -\left(N_s - 1\right)$ corrects the $(N_s + 1)$ scaling of the original. Since every module in the series string carries the same current, the pack current equals the module current and the pack capacity is 54 Ah.

3.4 PV array, boost converter and MPPT

Each panel (60 cells) is described by the single-diode model with $R_s = 0$ and ideality factor $n = 1.5$:

$$\begin{aligned} I &= I_{ph} - I_0\left[\exp\left(\frac{V}{N_c n V_t}\right) - 1\right], \\ I_{ph} &= I_{sc}\frac{G}{1000}\left[1 + \alpha_I (T - 25)\right], \\ I_0 &= \frac{I_{sc}}{\exp\left(\frac{V_{oc}}{N_c n V_t}\right) - 1}. \end{aligned} \tag{12}$$

The array has $N_s = 16$ panels in series and $N_p = 4$ strings (225.1 W panels, 14.41 kWp, $V_{mpp} = 478.4$ V at standard test conditions). The number of panels per string follows from the minimum boost input voltage $V_{in,\min} = V_{dc,avg}\left[1 - 0.8 D_{\max}\right] = 377.6$ V with $D_{\max} = 0.66$ and the hot-panel voltage 24.47 V. The boost converter and the P&O MPPT obey

$$V_o = \frac{V_{pv}}{1 - D}, \qquad L_b = \frac{V_{mpp}\, D_{\max}}{I_{in}\, \Delta I\, f_{sw}} = 10.5\ mH \tag{13}$$

$$V_{ref}(k+1) = V_{ref}(k) + \Delta V\ sign\left[\left(P_k - P_{k-1}\right)\left(V_k - V_{k-1}\right)\right], \quad \Delta V = 0.01 V_{mpp} \tag{14}$$

with an update period of 5 ms and V_{ref} limited to 0.8–1.1 V_{mpp}. The maximum power $P_{MPP}(G) = \max_V(V\,I)$ of the same array model is 14.87, 8.58 and 2.61 kW at 1000, 600 and 200 W/m^2.

3.5 Power balance of the hybrid station

$$P_{grid} + P_{pv} = P_{bat} + P_{loss} \tag{15}$$

Because the FEC regulates V_{dc}, any PV power reduces the grid import automatically, and a loss of PV power is supplied by the grid without changing the charging current.

4 Proposed BMS constrained charging algorithm

4.1 BMS rules

The BMS is implemented as a MATLAB Function block executed every $T_s = 1$ s (Fig. 3a). Its inputs, which pass through a unit delay, are the mean SOC, the highest cell voltage and the highest cell temperature:

$$SOC_{mean} = \frac{1}{6}\sum_{j=1}^{6} SOC_j, \qquad V_{\max} = \max_j v_{cell,j}, \qquad T_{\max} = \max_j T_j \tag{16}$$

The stage current is selected from four stages separated by three SOC breakpoints $s_1 < s_2 < s_3$:

$$I_{stage} = I_k \quad \text{for} \quad s_{k-1} \le SOC_{mean} < s_k, \qquad k = 1,\dots,4, \quad s_0 = 0,\ s_4 = 1 \tag{17}$$

A linear thermal derating reduces the current from 100 % at 40 °C to 20 % at 45 °C:

$$f_T = \begin{cases} 1, & T_{\max} \le 40\ ^\circ C \\ \max\left[0.2,\ 1 - 0.8\,\frac{T_{\max}-40}{5}\right], & T_{\max} > 40\ ^\circ C \end{cases} \tag{18}$$

A constant voltage (CV) loop acts on the highest cell voltage with anti windup

$$\begin{aligned} i_{cv} \leftarrow \min\Big\{ & 3C, \max\big[0, \min(i_{cv}, f_T I_{stage}) \\ & + K_{cv}(4.2 - V_{\max})\big]\Big\}, \qquad K_{cv} = 150\,A/V. \end{aligned} \tag{19}$$

$$I_{ref} = min\left(f_T\, I_{stage},\ i_{cv}\right) \tag{20}$$

Charging stops when $SOC_{mean} \ge 0.80$, and the elapsed time is the charging time $t_{20\to80}$. The algorithm therefore behaves as MSCC while the cells are far from their limits, as CV on the weakest cell near 4.2 V, and reduces the current when the hottest cell exceeds 40 °C. CCCV baselines are obtained with the same block by setting $I_1 = I_2 = I_3 = I_4$.

4.2 PSO formulation

The decision vector contains the four stage currents and three breakpoints,

$$\begin{aligned} &\mathbf{x} = [I_1, I_2, I_3, I_4, s_1, s_2, s_3], \qquad 27 \le I_k \le 162\,A, \\ &s_1 \in [0.25, 0.45], \qquad s_2 \in [0.40, 0.60], \qquad s_3 \in [0.55, 0.75]. \end{aligned} \tag{21}$$

where 27 to 162 A corresponds to 0.5C to 3C. Each candidate is evaluated by a full 20 → 80 % simulation and the cost

$$J(\mathbf{x}) = t_{20\to80} + 10\max(0,\, T_{peak} - 45) + 100\max(0,\, V_{peak} - 4.2) \tag{22}$$

is minimised, with $J = 1000$ if 80 % SOC is not reached within 3 h. The standard PSO update [48] is used:

$$\mathbf{v}_i \leftarrow w\,\mathbf{v}_i + c_1 r_1\,(\mathbf{p}_{best,i} - \mathbf{x}_i) + c_2 r_2\,(\mathbf{g}_{best} - \mathbf{x}_i)\,, \qquad \mathbf{x}_i \leftarrow clip\,(\mathbf{x}_i + \mathbf{v}_i,\, \mathbf{lb},\, \mathbf{ub}) \tag{23}$$

with $w = 0.7$, $c_1 = c_2 = 1.5$, 8 particles and 8 iterations (Fig. 3b). Two particles are seeded with the CCCV (100 A) and a hand designed MSCC profile, and the random generator is fixed for reproducibility. Simulink Fast Restart reduces each evaluation to about 2.5 s.

5 Simulation set up

5.1 Parameters and cases

The main parameters are listed in Table 2 and the simulation cases in Table 3. The switching level station models use the ode23t solver with a maximum step of 20 µs; grid side quantities are evaluated over the last 10 grid cycles of 0.4 s runs (0.10 to 0.20 s for the 0.2 s baseline run). The full 20 → 80 % charge is simulated with an averaged charging model in which the DC to DC converter is represented by an ideal controlled current source this is justified because the switching model regulates the charging current with about 2 % rms ripple (Section 6.3). This model uses the daessc solver with a maximum step of 2 s.

Table 2: Main simulation parameters

Sub system	**Parameter**	**Value**
Grid	Line voltage / frequency	415 V / 50 Hz
Front end converter	Rating / switching frequency	75 A DC (60 kW) / 10 kHz
	Line L / R (original)	0.3 mH / 20 mΩ (0.1 mH / 20 mΩ)
	DC link voltage / capacitance	800 V / 20 mF
Isolated DC to DC	Switching frequency / transformer ratio	10 kHz / 1 : 0.5

Sub-system	Parameter	Value
	Output inductance / PI gains	5 mH / $K_p = 2$, $K_i = 1$
Battery cell	Capacity / R_0 range	27 Ah / 8.2–11.7 mΩ
	Thermal mass / cell module resistance	900 J/K / 0.5 K/W
Pack	Configuration / capacity / OCV range	99s2p / 54 Ah / 346–415 V
	Initial SOC / cooling	0.20 / h = 100 W m^{-2} K^{-1}, A = 0.04 m^2
PV array	Configuration / rating	4 strings × 16 panels × 225.1 W / 14.41 kWp
Boost and MPPT	Frequency / inductor / MPPT	10 kHz / 10.5 mH / P&O, 5 ms, 1 % step
BMS	Sample time / voltage limit / derating	1 s / 4.2 V (K_{cv} = 150 A/V) / 40–45 °C, min 20 %
PSO	Particles × iterations / w, c_1, c_2	8 × 8 / 0.7, 1.5, 1.5

Table 3: Simulation cases

Case	Model	Condition	Purpose
Original FE	Station, two level FEC	L = 0.1 mH, 0.2 s	power quality before improvement battery indicators
Screening	Station, two and three level FEC	designs D1 to D5 of L, gains, converter; 0.2 s	front end design
H0	Station, two level FEC	improved FE, grid only, 0.4 s	power quality after improvement
H1	Hybrid, two level FEC	improved FE, PV at 1000 W/m^2	hybrid power quality and power sharing
H2 to H4	Hybrid, averaged FEC	PV at 1000 / 600 / 200 W/m^2	MPPT efficiency, renewable share, DC link
C1 to C3	Charging model	CCCV at 54, 100, 108 A (1C, 1.85C, 2C)	baselines
C4	Charging model	MSCC 135 / 108 / 81 / 54 A, breakpoints 0.35 / 0.50 / 0.65	hand designed MSCC
C5	Charging model	MSCC optimized by PSO	proposed algorithm

Case	Model	Condition	Purpose
Ambient	Charging model	25 °C (all); 35 and 45 °C (C1, C2, C4, C5)	climate sensitivity

5.2 Performance indices

Harmonics are obtained by FFT of the grid currents over an integer number of cycles, so that every harmonic falls on an FFT bin [43]. The current distortion is referred both to the fundamental current I_1 (THD) and to the rated demand current $I_L = 60\ kW/\left(\sqrt{3}\cdot 415\ V\right) = 83.5$ A (TDD):

$$THD_I = \frac{\sqrt{\sum_{h=2}^{50} I_h^2}}{I_1} \times 100\,\%, \qquad TDD = \frac{\sqrt{\sum_{h=2}^{50} I_h^2}}{I_L} \times 100\,\% \tag{24}$$

$$DPF = cos\varphi_1, \qquad PF = \frac{P}{S} = \frac{P}{3\,V_{rms} I_{rms}} \tag{25}$$

The TDD limit is 5 %, and the individual odd harmonic limits are 4 % ($h < 11$), 2 % (11–16), 1.5 % (17–22), 0.6 % (23–34) and 0.3 % (35–50) of I_L, with even harmonics limited to 25 % of these values. The hybrid operation and the charging performance are evaluated by

$$\eta_{MPPT} = \frac{\overline{v_{pv} i_{pv}}}{P_{MPP}(G)} \times 100\,\%, \qquad RE = \frac{P_{pv}}{P_{pv} + P_{grid}} \times 100\,\%, \qquad \eta_{st} = \frac{P_{bat}}{P_{grid} + P_{pv}} \tag{26}$$

$$\Delta t = \frac{t_{ref} - t}{t_{ref}} \times 100\,\% \tag{27}$$

$$S = \frac{1}{3600} \int |i_{cell}| \exp\left[\frac{E_a}{R_g}\left(\frac{1}{T_{ref}} - \frac{1}{T}\right)\right] dt, \qquad E_a = 31.5\,kJ/mol, \quad T_{ref} = 298.15\,K. \tag{28}$$

where S is an Arrhenius weighted ampere hour throughput used as an indicative ageing stress index. The PV share of one charge is $\int min\left(P_{bat}, P_{pv}\right)\, dt / \int P_{bat}\, dt$.

6 Results and discussion

6.1 Battery pack and BMS indicators

At 100 A the pack charges at 1.85C with a pack voltage of 401.8 V, i.e. 4.06 V per cell. This agrees with the cell model the OCV near 20–25 % SOC is about 3.62 V and the ohmic rise is 51.1 A × 8.6 mΩ = 0.44 V. The capacity and resistance deviations make the two cells of each parallel assembly share current unequally, the current spread is 1.19 A (2.3 % of the mean) and the voltage spread 9.0 mV. The simulated initial heating rate (0.229 K/s and 100 J/K thermal mass) agrees with the hand calculation $i^2 R_0 / \left(m c_p\right) = 0.225$ K/s within 2 %, which validates the thermal model. These cell

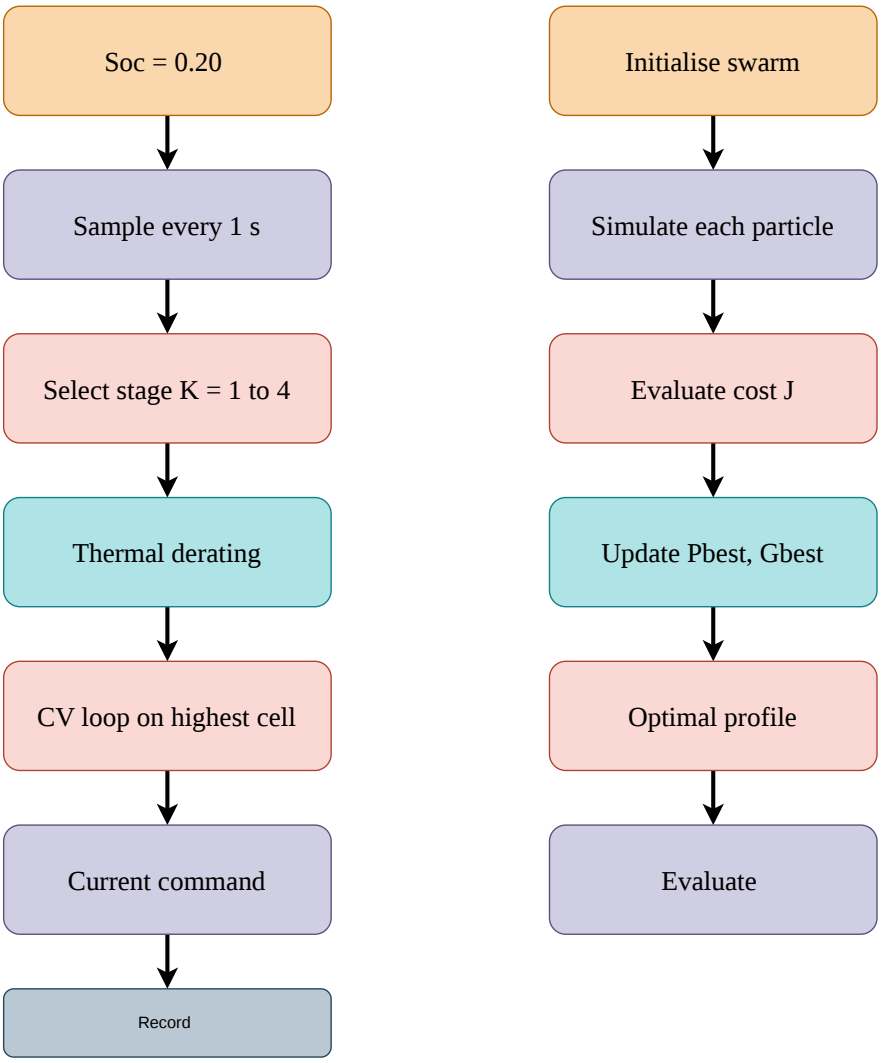


Fig. 3 (a) Flowchart of the BMS charging algorithm executed every 1 s (b) PSO procedure for optimizing the stage currents and SOC breakpoints

level quantities are exactly what the BMS must supervise, because the weakest and the hottest cell set the allowed charging current.

6.2 Front end design and grid power quality

Table 4 lists the front end designs that were screened with short 0.2 s runs at 100 A charging current. With the original 0.1 mH inductor (D1) the switching ripple is

too large (THD 12.35 %), and the three level converter with the same inductor (D4) reduces the THD only to 8.67 % at the cost of more switches. The design with $L = 0.3$ mH, the gains of (4) and the PI zero placed on the plant pole ($T_{i,i} = L/R$) gives the lowest distortion (D2) and was selected; it lies well below the admissible inductance of 1.57 mH. Halving the gain and removing the pole zero cancellation together (D3) raises the THD to 6.24 %. With 0.5 mH and 1.2 mH (D5) the current and DC link voltage loops interacted and the DC link voltage oscillated, with a peak to peak ripple of 0.85 to 1.0 % instead of 0.05 %, so no THD is reported for these runs. They were not retuned, because D2 already met the IEEE 519 TDD limit with margin with a smaller and cheaper inductor the retuning of the voltage loop for larger inductors is left for future work. The screening THD of D2 (3.26 %) differs slightly from the final value in Table 5 (3.67 %) because the final run is longer (20 cycles, window of the last 10 cycles).

Table 4: Front-end design alternatives (100 A charging current; 0.2 s screening runs; final values of the selected design in Table 5)

Design	L **(mH)**	**Current-loop gain**	**Pole–zero cancellation**	**Converter**	**Grid-current THD (%)**	**Result**
D1 (original)	0.1	Eq. (4)	yes	two-level	12.35	ripple too high
D2	**0.3**	**Eq. (4)**	**yes**	**two-level**	**3.26**	**selected**
D3	0.3	0.5 × Eq. (4)	no	two-level	6.24	slower loop, higher THD
D4	0.1	Eq. (4)	yes	three-level	8.67	ripple too high, more switches
D5	0.5 / 1.2	Eq. (4) and reduced	yes	two-level	–	DC-link oscillation; not retuned

Figure 4 compares the grid currents with the original and the improved front end, and Table 5 and Fig. 5 summarise the power quality. The improvement reduces the grid current THD from 13.54 % to 3.67 % and the TDD from 9.71 % to 2.66 %, well inside the 5 % IEEE 519 limit. With PV the grid supplies less current (38.6 A instead of 59.9 A), so the THD referred to I_1 rises to 6.33 %, while the TDD the index limited at 2.91 %. The true power factor rises from 0.956 to 0.991, the current unbalance falls from 1.50 % to 0.04 %, and the 7th harmonic, which exceeded its limit before (5.82 % of I_L), falls to 0.41 %. The true power factor (0.991) is slightly lower than the value

implied by the THD alone (≈ 0.999) because the switching ripple around 10 kHz, which lies above the 50th harmonic, is included in I_{rms} but not in the THD.

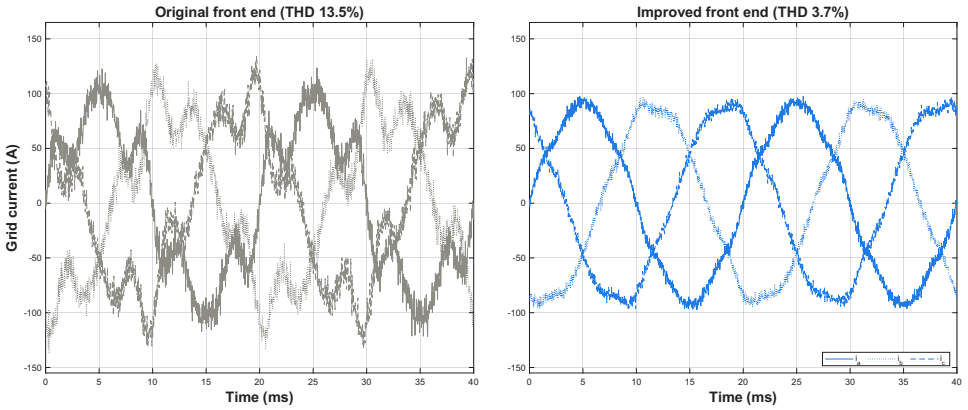


Fig. 4 Grid phase currents over the last two cycles (a) original front end (b) improved front end

Table 5: Grid power quality of the switching runs (last 10 cycles; I_L = 83.5 A)

Quantity	**Original FE**	**Improved FE (H0)**	**Improved FE + PV (H1)**	**Limit**
THD, % of I_1	13.54	3.67	6.33	–
Fundamental current I_1 (A rms)	61.6	59.9	38.6	–
TDD, % of I_L	9.71	**2.66**	**2.91**	5
Voltage THD at PCC (%)	0.003	0.011	0.003	8
Displacement PF	1.000	1.000	1.000	–
True PF	0.956	0.991	0.983	–
Current unbalance (%)	1.50	0.04	0.41	2
Odd / even harmonics above individual limit	12 / 23	4 / 13	3 / 14	0
Largest odd-harmonic excess (% of I_L)	h37: 1.72 vs 0.3	h35: 0.35 vs 0.3	h35: 0.54 vs 0.3	–

The individual harmonic check in Fig. 5b shows that all low order harmonics are within their limits after the improvement, but four high order odd harmonics (h25 to h35, largest 0.35 % against 0.3 %) and several small even components (below 0.55 % of I_L) remain above the strict individual limits. These orders lie where a plain L filter provides little attenuation; an LCL filter is the standard remedy. The station therefore meets the IEEE 519 TDD limit, and full individual harmonic compliance is left to the filter design listed in Section 7. The voltage THD and unbalance are very small because the grid is modelled as a stiff, balanced source.

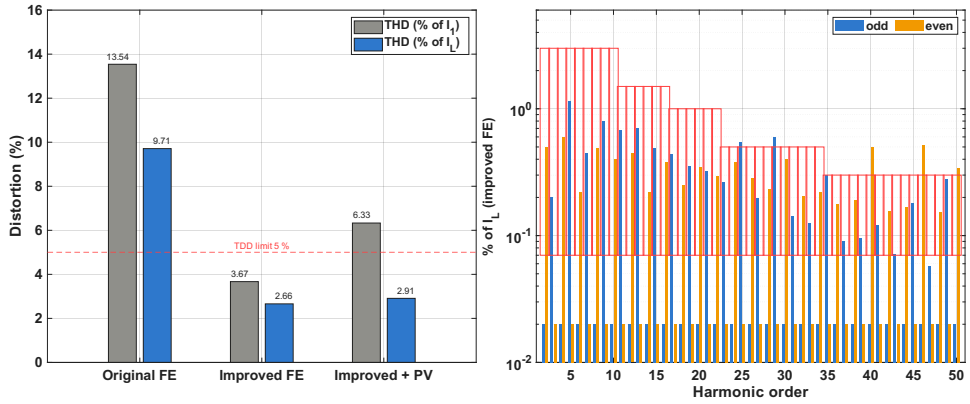


Fig. 5 (a) Grid current THD and TDD before and after the front end improvement and with PV, (b) individual harmonics of the improved front end against limits

6.3 DC link and charging current

The DC link is held at 800.0 V in every case, with a peak to peak ripple of 0.035 to 0.084 % (Table 6, Fig. 6a). The charging current is regulated at about 102 A with an rms ripple of 1.9 to 2.1 % (Fig. 6b), below the 2.5 % reported in [40]. The battery power (40.9 to 41.0 kW) is the same with and without PV, which confirms that the DC link voltage loop decouples the battery from the energy source.

6.4 PV grid hybrid operation

Table 6 and Fig. 7 summarise the hybrid operation. The P&O MPPT reaches the maximum power point within about 0.05 s (Fig. 6c) and extracts 98.2 to 98.3 % of the available power at every irradiance, where the available power is the maximum of the same PV model rather than the nameplate rating. At full sun the array supplies 14.6 kW, the grid import falls from 43.1 kW to 27.2 kW, and 34.9 % of the station input is renewable at 600 and 200 W/m^2 the renewable share is 20.2 % and 6.2 %. The station efficiency of 97 to 98 % is indicative because the semiconductor switches are ideal.

Table 6: DC link and PV–grid power sharing (last 10 cycles of 0.4 s runs)

Quantity	**H0 grid only**	**H1 1000 W/m² (two-level)**	**H2 1000 W/m²**	**H3 600 W/m²**	**H4 200 W/m²**
Available PV power P_{MPP} (kW)	–	14.87	14.87	8.58	2.61
PV power delivered (kW)	0	14.62	14.62	8.43	2.57
MPPT efficiency (%)	–	98.3	98.3	98.3	98.2
Grid power (kW)	43.1	27.7	27.2	33.3	39.1
Battery power (kW)	41.0	41.0	40.9	40.9	40.9

Quantity	H0 grid only	H1 1000 W/m² (two-level)	H2 1000 W/m²	H3 600 W/m²	H4 200 W/m²
Renewable share (%)	0	34.5	34.9	20.2	6.2
Station efficiency (%, ideal switches)	95.3	96.8	97.8	98.1	98.2
DC link ripple pk to pk (%)	0.048	0.042	0.035	0.084	0.080
Charging current ripple rms (%)	2.07	2.00	1.94	1.94	1.94

6.5 Charging algorithm comparison

Table 7 and Fig. 8 compare the five charging algorithms at 25 °C. The PSO optimized profile reaches 80 % SOC in 22.6 min, which is 38.1 % faster than 1C CCCV (36.5 min), 6.1 % faster than CCCV at the station current of 100 A (24.0 min), 3.4 % faster than 2C CCCV and 11.6 % faster than the hand designed MSCC. It respects both BMS limits the highest cell voltage is 4.201 V and the hottest cell reaches 43.5 °C. The durations are consistent with simple checks at 1C the ideal constant current time for 60 % SOC is 36 min, and at 1.85C it is 19.4 min, to which the CV taper adds about 4.6 min. The charge delivered in every case is 32.6 Ah, i.e. about 60 % of 54 Ah.

Table 7: Charging algorithms at 25 °C ambient (20 → 80 % SOC, 54 Ah pack)

Algorithm	$t_{20\to80}$ (min)	Δt vs CC-CV 1C (%)	Δt vs CC-CV 1.85C (%)	T_{peak} (°C)	V_{peak} (V)	ΔSOC at 80 % (%)	Stress S (Ah)
CC-CV 1C (54 A)	36.49	–	-51.7	33.9	4.200	3.45	20.5
CC-CV 1.85C (100 A)	24.05	34.1	–	41.6	4.201	3.92	25.9
CC-CV 2C (108 A)	23.39	35.9	2.8	42.4	4.201	3.94	26.8
MSCC fixed (135/108/81/54 A)	25.54	30.0	-6.2	41.3	4.207	3.86	26.7
MSCC-PSO (proposed)	**22.58**	**38.1**	**6.1**	**43.5**	**4.201**	**3.97**	**27.9**

The PSO found a limit riding profile, $\mathbf{I} = [125.7, 162.0, 158.2, 152.2]$ A with breakpoints [0.450, 0.492, 0.732] a moderate first stage ($\approx$ 2.3C) keeps the early temperature rise low, and the later stages are set near the 3C bound so that the CV loop and

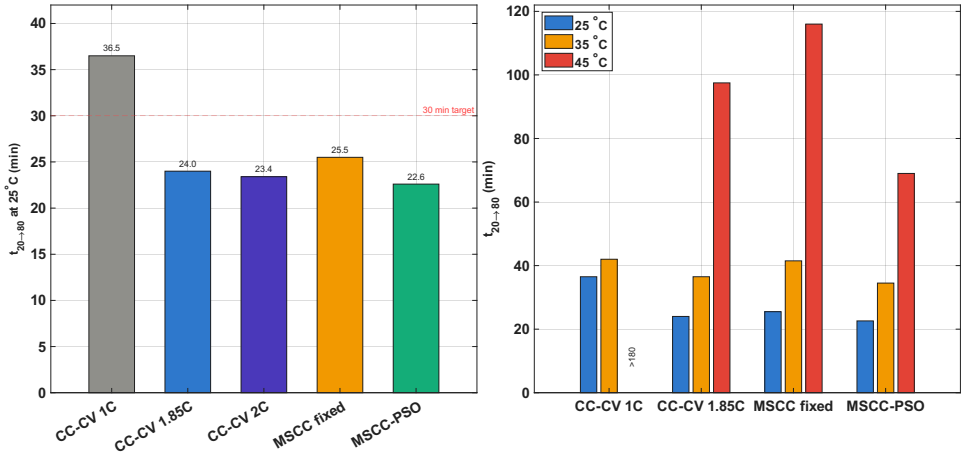


Fig. 6 Hybrid operation at 1000 W/m^2 (two level FEC) (a) DC link voltage (b) battery charging current (c) PV power and the model maximum power

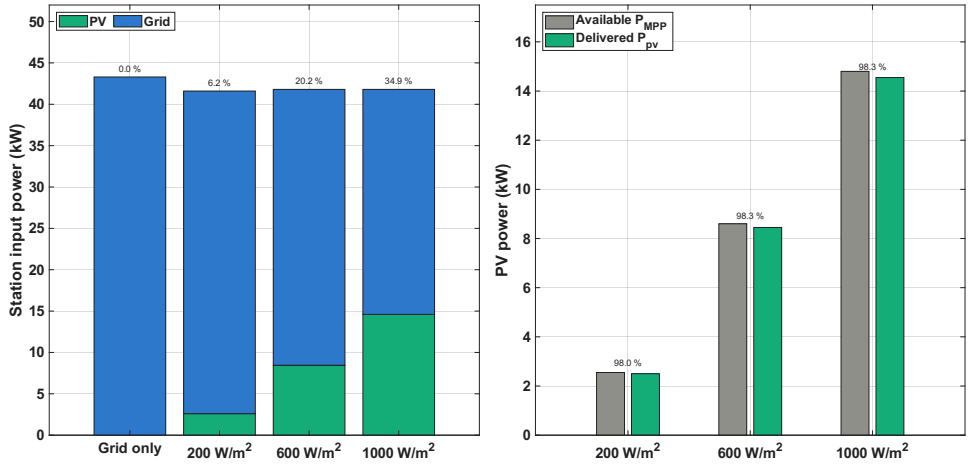


Fig. 7 (a) Station input power supplied by PV and grid, with the renewable share (b) available and delivered PV power with the MPPT efficiency

the thermal derating, not the stage values, determine the current (Fig. 8a). The hand designed decreasing MSCC is slower than simple CCCV at 1.85C its 135 A first stage is clipped by the 4.2 V limit, which also causes a single sample peak of 4.207 V, and its later stages (81 A and 54 A) are lower than the voltage and temperature limits would allow. This shows that stage currents and breakpoints must be optimized together with the BMS limits. The PSO converged within eight iterations, the best cost falling from 24.13 to 22.67 (Fig. 10a).

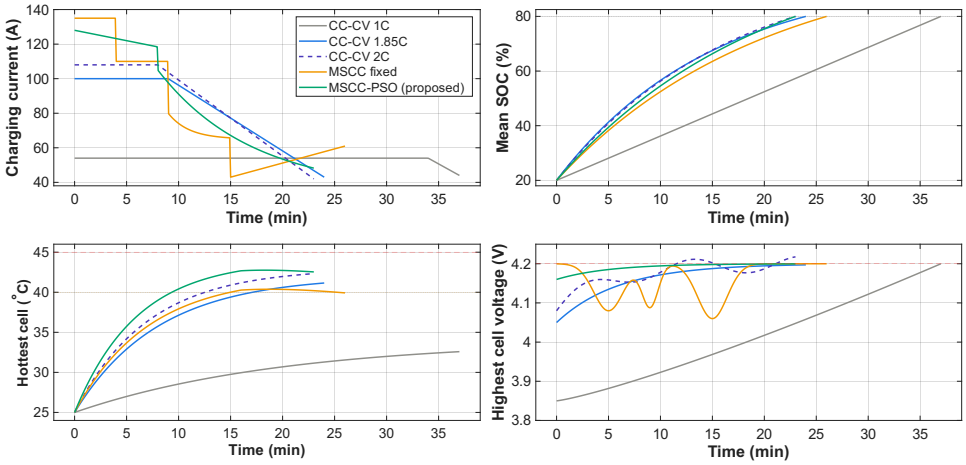


Fig. 8 Charging algorithms at 25 °C: (a) charging current; (b) mean SOC (c) hottest-cell temperature (d) highest cell voltage

6.6 Effect of ambient temperature and trade offs

Table 8 and Fig. 9 show the charging time at 25, 35 and 45 °C. A higher ambient temperature reduces R_0 but leaves less thermal headroom, so derating dominates. The profile remains the fastest at every temperature: 34.7 min at 35 °C (4.9 % less than CCCV 1.85C) and 68.7 min at 45 °C (29.8 % less), while 1C CCCV does not reach 80 % within 3 h at 45 °C because the derated current is only 20 % of the stage value. At 45 °C ambient no algorithm can keep the cells below 45 °C, because they cannot be cooled below the air temperature (48.7 °C peak for the profile), stations in hot climates therefore need pre cooling or liquid cooling, while the comparison of charging times remains valid.

Table 8: Charging time (min) at three ambient temperatures

Algorithm	25 °C	35 °C	45 °C	Gain of MSCC-PSO at 45 °C
CC-CV 1C	36.5	42.4	> 180 (80 % not reached)	> 62 %
CC-CV 1.85C	24.0	36.5	97.8	29.8 %
MSCC fixed	25.5	41.6	116.2	40.9 %
MSCC-PSO (proposed)	**22.6**	**34.7**	**68.7**	–

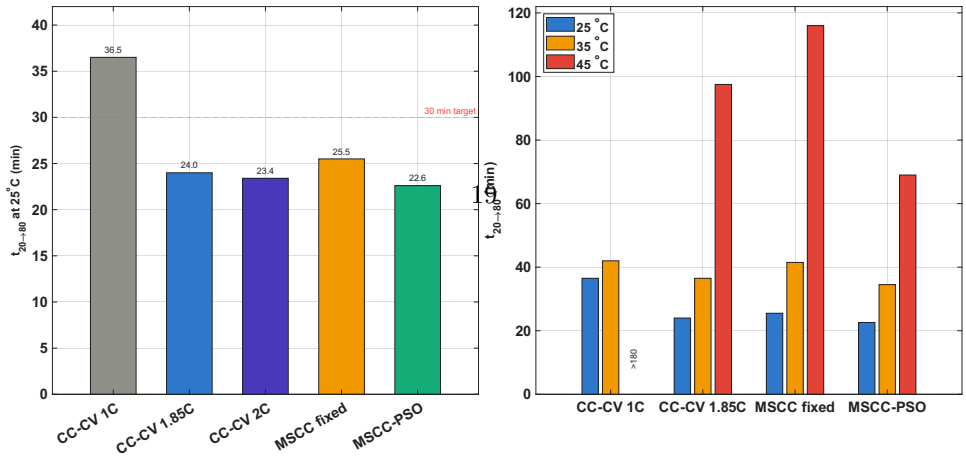


Fig. 9 Charging time from 20 % to 80 % SOC: (a) all algorithms at 25 °C with the 30 min fast-charge target [2, 32]; (b) effect of ambient temperature

Faster charging has a price. The Arrhenius weighted stress index (28) of the proposed profile is 7.7 % higher than that of CCCV 1.85C, and the SOC spread between cells at 80 % grows slightly from 3.92 % to 3.97 %. Figure 10b shows the resulting

speed temperature trade off every algorithm that is faster than 1C CCCV operates closer to the thermal limit, and the profile uses the available margin most completely. The weights of the PSO cost (22) can be tuned to trade charging time against ageing.

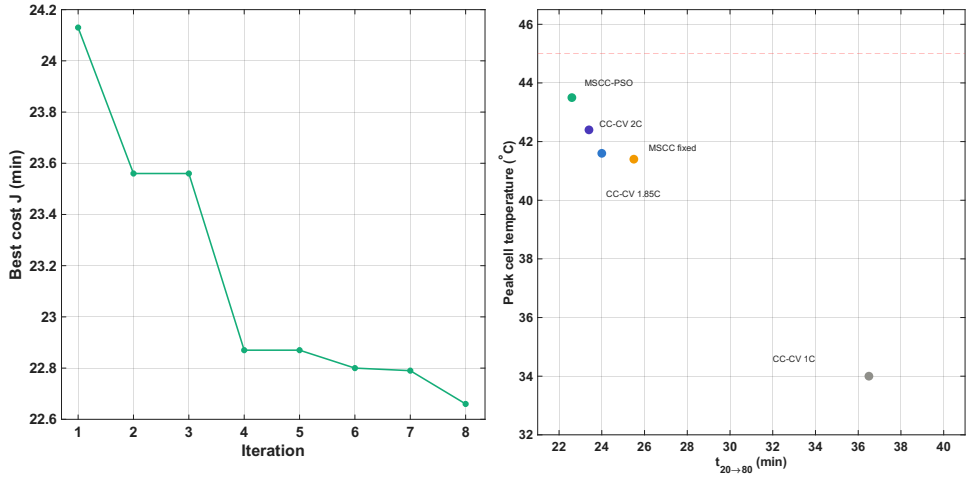


Fig. 10 (a) PSO convergence of the best cost; (b) charging time against peak cell temperature at 25 °C

A slower charge uses a larger share of solar energy because the vehicle stays longer With the PV powers measured in H2 to H4, the proposed profile takes 40.7 %, 23.5 % and 7.2 % of its 13.5 kWh charging energy from the 14.4 kWp array at 1000, 600 and 200 W/m^2, compared with 69.0 %, 39.8 % and 12.1 % for 1C CCCV. The operator can therefore choose between the fastest charge for the driver and a slower charge with more solar energy.

6.7 Comparison with published work

The results with published values and standard limits. Because the cited studies use different power levels, cells and test conditions, the comparison is indicative, and the conditions of each study are listed. The TDD satisfies limit with and without PV, whereas four high order odd harmonics and thirteen small even harmonics remain marginally above their individual limits (largest excess at the 35th harmonic, 0.35 % of I_L against 0.3 %, and 0.54 % with PV), an LCL filter is planned to remove them (Section 7). The THD of 3.67 % is lower than the 7.89 % reported for an 80 kW DC fast charger [39], but higher than that of the 10 kW MPC charger in [40] and the 350 W ANN controlled converter in [36], which use advanced control at much smaller power. The charging time reduction of 38.1 % against 1C CCCV is larger than the 31.2 % reported for the PSO multi stepped CCCV in [46], although [46] charges a single cell to 100 % SOC. Against CCCV at equal peak current, the 6.1 % reduction at 25 °C lies within the 1.9 to 9.54 % range of [47], and it grows to 29.8 % at 45 °C where thermal derating dominates. The 20 to 80 % charge takes 22.6 min, within the

30 min fast charging target of [2, 32]. The MPPT efficiency of 98.2 to 98.3 % adds PV tracking evidence that the base station study [10] did not report.

7 Limitations and future scope

The results should be read with the following limitations, which also define the future work.

1. The front end uses an L filter; a few high order odd and small even harmonics exceed the strict individual limits. An LCL filter will be designed to achieve full individual harmonic compliance, together with a retuned DC link voltage loop that allows larger inductances (0.5–1.2 mH, design D5 in Table 4).
2. At 600 and 200 W/m^2 the P&O step (1 % of V_{mpp} every 5 ms) interacts with the DC link voltage loop, so the averaged runs at these irradiances were used only for PV power, MPPT efficiency and renewable share. A slower perturbation (20 ms) and a variable step or incremental conductance MPPT will be evaluated for the grid side analysis at partial irradiance.
3. The semiconductor switches are ideal, so efficiencies are indicative, switching level runs cover 0.4 s, and the full charge uses an averaged charger.
4. The ageing stress index is indicative, coupling the optimization with an electrochemical or semi empirical ageing model would allow a quantitative speed lifetime trade off and a multi objective (Pareto) PSO.
5. At 45 °C ambient active pre cooling is required, a coupled thermal management and charging optimization will be studied.
6. Hardware in the loop and experimental validation on a scaled charger and a 3s2p module are planned.

8 Conclusions

This paper presented a BMS constrained, PSO optimized multistage charging algorithm for an EV battery in a PV grid hybrid DC fast charging station and evaluated it together with the station's power quality. The main findings are

1. A realistic 99s2p, 54 Ah pack of temperature dependent cells charges at 1.85C and 4.06 V per cell in the station, its thermal model agrees with hand calculation within 2 %, and cell level spreads (2.3 % current, 9 mV voltage) are available to the BMS.
2. Rerating the front end converter to the actual charging power and selecting a 0.3 mH line inductance reduces the grid current TDD from 9.71 % to 2.66 % (2.91 % with PV), within the IEEE 519 limit, at a power factor of 0.991.
3. The P&O MPPT extracts 98.2 to 98.3 % of the available PV power and supplies 6.2 to 34.9 % of the station input at 200 to 1000 W/m^2, while the 800 V DC link and the charging current remain unaffected.
4. The PSO optimized MSCC profile charges from 20 % to 80 % SOC in 22.6 min — 38.1 % faster than 1C CCCV and 6.1 % faster than CCCV at equal peak current with the highest cell at 4.201 V and 43.5 °C; at 45 °C ambient it is 29.8 % faster than CCCV.

5. The price of faster charging is a 7.7 % higher indicative ageing stress, which can be balanced through the PSO cost weights.

The study shows that the charging profile and the grid side power quality of a hybrid station can be designed together within cell level BMS limits. The work will add an LCL filter, a slower or adaptive MPPT, an ageing model in a multi objective optimization and hardware validation.

Acknowledgements. The authors thank Sharda University, Greater Noida, for providing the licensed MATLAB/Simulink R2026b software (The MathWorks, Inc.) used for all modelling and simulations in this work.

Declarations.

Funding. The authors did not receive support from any organization for the submitted work. No funding was received for conducting this study.

Data availability. The simulation models, scripts and data generated during this study are available from the corresponding author on reasonable request.

Author contributions. A.S.: conceptualization, methodology, modelling and simulation, formal analysis, visualization, writing – original draft. S.D.: conceptualization, supervision, validation, writing , review and editing. M.R.: supervision, validation, resources, writing review and editing. All authors read and approved the final manuscript.

Competing interests. The authors declare no competing interests.

Ethics approval and consent to participate. Not applicable.

Consent for publication. Not applicable.

Clinical trial number. Not applicable.

References

[1] Rivera S, Goetz SM, Kouro S, Lehn PW, Pathmanathan M, Bauer P, et al. Charging infrastructure and grid integration for electromobility. Proc IEEE. 2023;111(4):371–96. https://doi.org/10.1109/JPROC.2022.3216362

[2] Brenna M, Foiadelli F, Leone C, et al. Electric vehicles charging technology review and optimal size estimation. J Electr Eng Technol. 2020;15:2539–52. https://doi.org/10.1007/s42835-020-00547-x

[3] Leone C, Longo M. Modular approach to ultra-fast charging stations. J Electr Eng Technol. 2021;16:1971–84. https://doi.org/10.1007/s42835-021-00757-x

[4] Bhatti AR, Tamoor M, Liaqat R, Rasool A, Salam Z, Ali A, et al. Electric vehicle charging stations and the employed energy management schemes: a classification based comparative survey. Discov Appl Sci. 2024;6(10). https://doi.org/10.1007/s42452-024-06190-9

[5] Rana R, Saggu TS, Letha SS, et al. V2G based bidirectional EV charger topologies and its control techniques: a review. Discov Appl Sci. 2024;6:588. https://doi.org/10.1007/s42452-024-06297-z

[6] Reddy BN, Jyothi B, Rao GS, et al. State-of-the-art DC-DC converters for electric mobility and renewable integration: trends, challenges, and future directions. Discov Appl Sci. 2026;8:160. https://doi.org/10.1007/s42452-025-08120-9

[7] Rajendran G, Vaithilingam CA, Naidu K, et al. Energy-efficient converters for electric vehicle charging stations. SN Appl Sci. 2020;2:583. https://doi.org/10.1007/s42452-020-2369-0

[8] Tamba JS II, Abdulkarim A, Shuaibu AN. Solar powered electric vehicle charging system: a comprehensive review. Discov Electron. 2025;2:96. https://doi.org/10.1007/s44291-025-00139-x

[9] Hossain MN, Cho HM. Techno-economic feasibility of photovoltaic-powered electric vehicle charging stations: a global review and future outlook. Sustain Energy Res. 2026;13:9. https://doi.org/10.1186/s40807-025-00228-1

[10] Singla P, Boora S, Singhal P, Mittal N, Mittal V, Gared F. Design and simulation of 4 kW solar power-based hybrid EV charging station. Sci Rep. 2024;14:7336. https://doi.org/10.1038/s41598-024-56833-5

[11] Singh S, Chauhan P, Singh NJ. Feasibility of grid-connected solar-wind hybrid system with electric vehicle charging station. J Mod Power Syst Clean Energy. 2021;9(2):295–306. https://doi.org/10.35833/MPCE.2019.000081

[12] Singh B, Verma A, Chandra A, Al-Haddad K. Implementation of solar PV-battery and diesel generator based electric vehicle charging station. IEEE Trans Ind Appl. 2020;56(4):4007–16. https://doi.org/10.1109/TIA.2020.2989680

[13] Jain V, Singh B, Seema. A grid connected PV array and battery energy storage interfaced EV charging station. IEEE Trans Transp Electrif. 2023;9(3):3723–30. https://doi.org/10.1109/TTE.2023.3234994

[14] Shukl P, Singh B. Distributed energy resources based EV charging station with seamless connection to grid. IEEE Trans Ind Appl. 2023;59(3):3826–36. https://doi.org/10.1109/TIA.2023.3239583

[15] Sekhar KSR, Chaudhari MA, Khadkikar V. Enhanced hybrid converter topology for PV-grid-EV integration. IEEE Trans Energy Convers. 2023;38(4):2634–46. https://doi.org/10.1109/TEC.2023.3287890

[16] El-Taweel NA, Farag H, Shaaban MF, AlSharidah ME. Optimization model for EV charging stations with PV farm transactive energy. IEEE Trans Ind Inform. 2022;18(7):4608–21. https://doi.org/10.1109/TII.2021.3114276

[17] Bagherwal S, Mahapatra S. Enhanced stability and control of solar powered EV charging stations using disturbance observer-based adaptive sliding mode control for DC voltage stabilization. IEEE Access. 2024;12:183293–311. https://doi.org/10.1109/ACCESS.2024.3511637

[18] Swamynathan K, Mahalingam N, Paramasivam A, Vijayalakshmi S. PV based off-grid charging station for E-vehicles using PWM and phase-shift controlled interleaved three-port converter. SN Appl Sci. 2023;5:331. https://doi.org/10.1007/s42452-023-05571-w

[19] Kancherla AB, Prasad NB, Kishore DR. Solar energy EV charging system using integrated Zeta-Luo converter. J Eng Appl Sci. 2024;71:147. https://doi.org/10.1186/s44147-024-00477-9

[20] Mazumdar D, Shuaibu HA, Sain C, Ustun TS. A novel and sturdy MPPT architecture for grid-tied EV charging stations using Ali Baba and forty thieves optimization. Discov Sustain. 2025;6:530. https://doi.org/10.1007/s43621-025-01089-w

[21] Karmakar A, et al. Techno-economic analysis and optimized PV-powered EV charging facilities under various climate conditions in India. Discov Sustain. 2025;6:285. https://doi.org/10.1007/s43621-025-01119-7

[22] Ahamed M, et al. Automated control integration of solar and wind energy for sustainable DC microgrid deployment in desert environments for EV charging. Discov Electron. 2026;3:46. https://doi.org/10.1007/s44291-026-00192-0

[23] Palanisamy S, Lala H. Optimal sizing of renewable energy powered hydrogen and electric vehicle charging station (HEVCS). IEEE Access. 2024;12:48239–54. https://doi.org/10.1109/ACCESS.2024.3383960

[24] Ullah Z, Yan L, Rehman AU, Qazi HS, Xiaodong W, Jingkuan L, et al. Distributed consensus-based optimal power sharing between grid and EV charging stations using derivative-free charging scheduling. IEEE Access. 2024;12. https://doi.org/10.1109/ACCESS.2024.3439019

[25] Ji D, Lv M, Yang J, Yi W. Optimizing the locations and sizes of solar assisted electric vehicle charging stations in an urban area. IEEE Access. 2020;8:112772–82. https://doi.org/10.1109/ACCESS.2020.3003071

[26] Reddy GH, Depuru SR, Gope S, Narayana BV, Bhukya MN. Simultaneous placement of multiple rooftop solar PV integrated electric vehicle charging stations for reliability benefits. IEEE Access. 2023;11:130788–801. https://doi.org/10.1109/ACCESS.2023.3335093

[27] Jiang Y, Ortmeyer T, Fan M. Data-driven fast uncertainty assessment of distribution systems with correlated EV charging demand and renewable generation.

IEEE Trans Sustain Energy. 2023;14(3):1446–56. https://doi.org/10.1109/TSTE.2023.3236446

[28] Shalaby M. Planning smart EV charging infrastructure around metro transit hubs in Riyadh. IEEE Access. 2025;13:201935–47. https://doi.org/10.1109/ACCESS.2025.3638158

[29] Gunasekaran R, Manjunatha B, Anand S, Pareek PK, Gupta S, Shukla A. Prediction of electric vehicle charging demand using enhanced gated recurrent units with RKOA based graph convolutional network. Discov Appl Sci. 2024;6:605. https://doi.org/10.1007/s42452-024-06326-x

[30] Mahfouz MM, Iravani MR. Grid-integration of battery-enabled DC fast charging station for electric vehicles. IEEE Trans Energy Convers. 2020;35(1):375–85. https://doi.org/10.1109/TEC.2019.2945293

[31] Mahfouz MM, Iravani R. A supervisory control for resilient operation of the battery-enabled DC fast charging station and the grid. IEEE Trans Power Deliv. 2021;36(4):2532–41. https://doi.org/10.1109/TPWRD.2020.3031859

[32] Arya H, Das M. Fast charging station for electric vehicles based on DC microgrid. IEEE J Emerg Sel Top Ind Electron. 2023;4(4):1204–12. https://doi.org/10.1109/JESTIE.2023.3285535

[33] Barsali S, Bojoi R, Ceraolo M, Mallemaci V, Mandrile F, Mocci S, et al. Grid forming inverters for electric vehicle charging stations to enhance distribution grid resilience. IEEE Access. 2025;13:109687–700. https://doi.org/10.1109/ACCESS.2025.3582070

[34] Nisha KS, Gaonkar DN. Model predictive controlled three-level bidirectional converter with voltage balancing capability for setting up EV fast charging stations in bipolar DC microgrid. Electr Eng. 2022;104:2653–65. https://doi.org/10.1007/s00202-022-01492-w

[35] Sangeetha EP, Subashini N, Lindiya SA, Uma D. A distinctive optimized sliding mode control approach for grid-connected bidirectional DC-DC converters in DC fast charging stations with G2V and V2G support. Electr Eng. 2026;108:262. https://doi.org/10.1007/s00202-026-03609-x

[36] Ashiq MMA, et al. Artificial neural network controlled canonical switching converter for electric vehicle charging applications. Neural Comput Appl. 2026;38:306. https://doi.org/10.1007/s00521-026-12009-y

[37] Dakka O, Patthi S, Rao JVGR, et al. A 5-kW unidirectional wireless power transfer EV charger with a novel multi-level PFC boost converter on front-end side. J Eng Appl Sci. 2024;71:7. https://doi.org/10.1186/s44147-023-00333-2

[38] Srivastava A, Manas M, Dubey RK. Electric vehicle integration's impacts on power quality in distribution network and associated mitigation measures: a review. J Eng Appl Sci. 2023;70:32. https://doi.org/10.1186/s44147-023-00193-w

[39] Rajkumar S, Balasubramanian R, Kathirvelu KP. A comparative analysis of supraharmonic emission by DC fast chargers used for electric vehicle charging. Sci Rep. 2025;15:7992. https://doi.org/10.1038/s41598-025-92049-x

[40] Tan AST, Ishak D, Mohd-Mokhtar R, et al. Predictive control of plug-in electric vehicle chargers with photovoltaic integration. J Mod Power Syst Clean Energy. 2018;6:1264–76. https://doi.org/10.1007/s40565-018-0411-7

[41] Verma A, Singh B. AFF-SOGI-DRC control of renewable energy based grid interactive charging station for EV with power quality improvement. IEEE Trans Ind Appl. 2021;57(1):588–97. https://doi.org/10.1109/TIA.2020.3029547

[42] Srilakshmi K, Kondreddi K, Ramadevi A, Muniraj R, Vangalapudi R. Grid connected and standalone renewable source fed UPQC: a hybrid control technique for power quality enhancement. Discov Appl Sci. 2025;7:147. https://doi.org/10.1007/s42452-025-06562-9

[43] IEEE Std 519-2014. IEEE recommended practice and requirements for harmonic control in electric power systems. New York: IEEE; 2014. https://doi.org/10.1109/IEEESTD.2014.6826459

[44] Shirguppikar S, Gavali P, Ganachari V, Jadhav P, Zubairuddin M, Khot S, et al. Characterization of Li-ion battery and state of charge estimation methods for diverse battery chemistries: a review. Discov Appl Sci. 2025;7:1443. https://doi.org/10.1007/s42452-025-07906-1

[45] Louis GA, Sampathkumar S. Predicting the state of charge of lithium ion battery in e-vehicles using Box-Jenkins combined artificial neural network model. Discov Appl Sci. 2025;7:129. https://doi.org/10.1007/s42452-024-06445-5

[46] Magdy M, Hanafy F, Abou-Zalam B, Nabil E. Optimized multi-stepped constant current constant voltage fast charging controller for lithium-ion batteries. Sci Rep. 2025;15:40359. https://doi.org/10.1038/s41598-025-25924-2

[47] Ye M, Gong H, Xiong R, Mu H. Research on the battery charging strategy with charging and temperature rising control awareness. IEEE Access. 2018;6:64193–201. https://doi.org/10.1109/ACCESS.2018.2876359

[48] Kennedy J, Eberhart R. Particle swarm optimization. In: Proceedings of ICNN'95 International Conference on Neural Networks, vol. 4. Perth: IEEE; 1995. p. 1942–8. https://doi.org/10.1109/ICNN.1995.488968

[49] The MathWorks Inc. DC fast charger for electric vehicle. Simscape Electrical example, MATLAB R2026b. Natick: The MathWorks Inc.; 2026. https://www.mathworks.com/help/simscape-electrical/ug/dc-fast-charger.html

[50] The MathWorks Inc. Apply temperature-dependent cell parameter variations to battery module. Simscape Battery example, MATLAB R2026b. Natick: The MathWorks Inc.; 2026. https://www.mathworks.com/help/simscape-battery/ug/apply-temperature-dependent-cell-parameter-variation-in-module.html

[51] The MathWorks Inc. Solar PV system with MPPT using boost converter. Simscape Electrical example, MATLAB R2026b. Natick: The MathWorks Inc.; 2026.